Supporting Information for "Atmospheric Contributions to Global Ocean Tides for Satellite Gravimetry"

Kyriakos Balidakis[1], Roman Sulzbach[1,2], Linus Shihora[1], Christoph Dahle[1], Robert Dill[1], Henryk Dobslaw[1]

[1]GFZ German Research Centre for Geosciences, Department 1: Geodesy, Potsdam, Germany

[2]Freie Universität Berlin, Institut für Meteorologie, Berlin, Germany

Corresponding author: K. Balidakis, GFZ German Research Centre for Geosciences, Department 1: Geodesy, Potsdam, Germany. (kyriakos.balidakis@gfz-potsdam.de)

October 25, 2022, 1:14pm

1. Stochastic Properties of Numerical Weather Model data and the Associated Harmonic Amplitudes

Estimates for the harmonic coefficients in eq. 1 of the main article are obtained by node-wise least-squares adjustments. While imposing stochastic equivalence constraints between estimates of tidal amplitudes at neighbouring grid nodes with a weight that decreases with distance yields tidal amplitudes with slightly larger spatial coherence, it is reciprocal to tacitly applying a smoothing filter that damps high-frequency (sub-degree) features that are inherent for example in the atmospheric response to the solar diurnal wave, thus not allowing to fully utilize the high-resolution ERA5 and ECMWFop fields. Therefore, the harmonic amplitudes at each node are estimated independently.

It is possible that assumptions about the error covariance of y assumed during the adjustment may affect the harmonic estimates. We studied whether it should be diagonal or fully-populated, and whether the observations' variance should vary over time. First, neglecting the fact that pressure values are correlated in time — hence assuming a diagonal observations' covariance matrix — yields largely deflated tidal harmonic estimate uncertainties, which hinders the statistical evaluation of the results. We calculated the auto-covariance for all native grid nodes and then fitted Hirvonen models (Hirvonen, 1962), that is,

$$y = \sigma_0 \left(1 + \left(\frac{dt}{\xi} \right)^2 \right)^{-1}, \tag{1}$$

where σ_0 is the signal variance and ξ is the correlation length. Figure S1 illustrates ξ and suggests that the decorrelation process may take several days and exhibits marked spatial variability. Moreover, temporal decorrelation is achieved slower for de-tided pressure

series, thus suggesting that the prediction thereof is facilitated. We note that ξ estimated from the MPIOM simulations does not display a consistent pattern in the tropics with reduced decorrelation lag in the Atlantic in comparison to the Pacific and Indian Ocean. This is attributed to the relatively higher power in variability at synoptic time scales induced by the cross-equatorial currents (e.g., the Atlantic equatorial undercurrent). We tested three weighing schemes: (i) applying the adjusted observations' covariance from a prior adjustment where an identity matrix was employed, (ii) applying the autocovariance itself by constructing a symmetric-Toeplitz-type weight matrix, and (iii) applying an approximation of the empirical autocovariance adopting Hirvonen's model in a symmetric-Toeplitz framework. To expedite computations, the symmetric-Toeplitz-type weight matrix is applied using the fast Fourier transform after embedding it into a circulant matrix. Second, unlike most NWMs, ERA5 provides the means to obtain uncertainty estimates for some parameters provided employing the scatter of the ten-member 4D-Var ensemble. However, comparing ERA5 pressure with in situ barometer data suggests that these figures are too optimistic. Two schemes were tested regarding the diagonal elements of the observations' covariance: (i) all observations have variance $10^4\,\mathrm{Pa}^2$, and (ii) the variance of each observation equals the scatter of the ensemble mean associated with the particular location and epoch. We found that any combination of the two schemes of obtaining the diagonal elements and the three schemes of obtaining the off-diagonal elements of the observations' covariance matrix yields differences that may be neglected. For instance, for the most important waves, that is, the S_1 and S_2, the amplitude differences do not differ by more than 5 Pa for 85 % and 96 % of the global cover, respectively. The largest differences are found in polar regions where the tidal amplitudes are insub-

stantial. The differences between the post-fit-residual scatter between all the scenarios is not statistically significant. The computational overhead from employing node-specific fully-populated covariance matrices is prohibitive for analyzing longer time series, as the epoch-wise normal equation stacking, which has minimum memory requirements, can no longer be employed. Moreover, eliminating systematic signals in the post-fit residuals becomes a crucial aspect should observations be considered correlated.

Simultaneous estimation of harmonic amplitudes for different waves does not corrupt the results. Analyzing the correlation between the harmonic terms (cosine with sine amplitude estimates as well as amplitude and phase estimates derived by uncertainty propagation) from the least-squares adjustment carried out for each grid node reveals that they do not contaminate each other. That is, setting up the harmonic coefficients of wave i does not affect the coefficients of wave j, provided that these waves fall under the ensemble tabulated in Table 1 of the main article. The largest correlation we found was between amplitudes of the semi-diurnal waves M_2 and T_2 which did not exceed the 0.0005 level. Moreover, harmonic amplitude estimates for the waves we selected from an adjustment where only those were set up as unknowns and another adjustment where the parameter space comprized waves spanning from the folding frequency (S_{12}) to one cycle per year (S_a) do not differ in a statistical manner ($p \leq 0.001$) and in no wave and no grid node exceed the 0.05 Pa level.

The harmonic coefficients' confidence intervals are important to assess the error budget in satellite gravimetry, as well as to potentially evaluate sea surface height ensemble scatter in a Monte Carlo framework. The harmonic coefficients' uncertainty is scaled by the a posteriori unit variance which in turn is a function of the post-fit residuals' magnitude,

should the weighting strategy be described by an identity matrix (see Section 2 of the main article for a discussion over the architecture of the stochastic model of the tidal fit). The lower the portion of the signal attributed to tidal variations, the higher the residuals' magnitude, hence the larger the uncertainty of the harmonic coefficients. The ratio of the largest over the smallest a posteriori unit variance for pressure render harmonic amplitudes at some sites 24 times more precisely estimated than others. For wind stress, we observe that the estimation unit variance is in almost all cases well below 1 (0.03, on average), which is indicative of overfiting and suggestive of a weak response to tidal forcing. However, these figures do not reflect the accuracy of the estimated coefficients rather than the efficiency of the deterministic model, that is, the ability of the ansatz (see equation 2 of the main article) to describe the signal under investigation; the quality of the underlying weather model cannot be considered whatsoever. While synoptic variations can be captured, e.g., by a Kalman filter whose state vector includes an instantaneous offset thus minimizing the extend to which unmodelled transient variations contribute to the estimates' uncertainty, the latter heavily depends on the subjective decision on the noise driving the stochastic processes that describe the harmonic amplitudes' and offsets' temporal variations, consequently yielding impractical uncertainty estimates. It is more appropriate to resort to external observations (e.g., barometers) in an effort to assign a reliable accuracy measure to harmonic estimates, a task to be undertaken in a future study.

2. Harmonic Coefficient Estimates of the 16 Partial Tides

2.1. Atmospheric Pressure

Figure S2 illustrates the ERA5-derived pressure amplitudes and phases of the 16 waves. We have also created a movie illustrating high-frequency pressure variations which may be retrieved from `https://nextcloud.gfz-potsdam.de/s/6LPbFQk3nNYcHbd`.

2.2. Meridional Surface Wind Stress

Figure S3 illustrates the ERA5-derived meridional surface wind stress amplitudes and phases of the 16 waves.

2.3. Zonal Surface Wind Stress

Figure S4 illustrates the ERA5-derived zonal surface wind stress amplitudes and phases of the 16 waves.

2.4. Ocean Bottom Pressure

Figure S5 illustrates the MPIOM-derived ERA5-forced ocean bottom pressure amplitudes and phases of the 16 waves.

3. High-Frequency Variability Explained by the 16 Partial Tides

Figure S6 illustrates the scatter of the atmospheric pressure, wind stress, and ocean bottom pressure at different frequency bands.

3.1. Atmospheric Pressure

Figure S7 illustrates the portion of the atmospheric pressure variance each wave of the ensemble is capable of explaining.

3.2. Meridional Surface Wind Stress

Figure S8 illustrates the portion of the meridional wind stress variance each wave of the ensemble is capable of explaining.

3.3. Zonal Surface Wind Stress

Figure S9 illustrates the portion of the zonal wind stress variance each wave of the ensemble is capable of explaining.

3.4. Ocean Bottom Pressure

Figure S10 illustrates the portion of the ocean bottom pressure variance each wave of the ensemble is capable of explaining.

4. Notes on the Temporal Modulation of Partial Tides

Solar and lunar declinations, fluctuations in the atmospheric ozone and water vapor, as well as variations in the type, the quality, the quantity, and the distribution of observations assimilated in numerical weather prediction models yield inter-annual and seasonal modulations in tidal amplitudes (e.g., Ray & Poulose, 2005; Ray & Merrifield, 2019). We have estimated time-dependent tidal amplitudes for the waves listed in Table 1 of the main article by modelling them as random walk processes, in the framework of a Dyer-McReynolds square-root information filter (e.g., Bierman, 2006). We calculate the signal-to-noise-ratio by employing the time-independent amplitude estimates from the batch least-squares adjustment and the scatter in the time-dependent amplitude estimate time series from the filter. Globally averaged signal-to-noise ratio (SNR) from ERA5, MERRA2 (Gelaro et al., 2017), and ECMWFop series have been computed as well for the same baseband. are shown in Fig. S11. We observe a good agreement between these three weather models (with the exception of the M_2 tide where ERA5 yields 23 dB and MERRA2 yields only 14 dB) and that the SNR is a weak function of the wave magnitude; the largest SNR values are found for S_2 (44 dB), S_1 (31 dB), T_3 (28 dB), R_3 (28 dB), and S_3 (24 dB). Moreover, ERA5-derived harmonics provide a SNR larger than ECMWFop across the spectrum, which we attribute to the fact that the former is a reanalysis product. This feature persists even after we match the logging interval and wave amplitudes solved for in analyzing ERA5 data. For all waves in the ensemble of choice the SNR is above 14 dB. An attempt to distinguish data assimilation artefact manifestations from the true modulation signal in high-frequency tidal amplitudes is elaborated in a follow-up study.

5. Dissemination of Atmospheric Pressure Tides and Ocean Bottom Pressure (or Sea Surface Height) Tides

To approximate the 2D fields (colatitude θ over longitude λ) of tidal cosine and sine amplitudes, we developed them into spherical harmonic series (e.g., Sneeuw, 1994)

$$f(\theta,\lambda) = \sum_{n=0}^{n_{max}} \sum_{m=0}^{n} \left(\overline{C}_{nm}\cos(m\lambda) + \overline{S}_{nm}\sin(m\lambda)\right)\overline{P}_{nm}(\cos(\theta)), \tag{2}$$

where $\overline{C}_{nm}$ and $\overline{S}_{nm}$ are the fully normalized Stokes coefficients for degree n and order m, and $\overline{P}_{nm}$ are the fully normalized associated Legendre functions. $n_{max} \to \infty$ is the maximum degree of the expansion. Instead of calculating directly the Stokes coefficients following

$$\begin{Bmatrix}\overline{C}_{nm}\\ \overline{S}_{nm}\end{Bmatrix} = \frac{1}{4\pi}\int_{\lambda=0}^{2\pi}\int_{\theta=0}^{\pi}\begin{Bmatrix}\cos(m\lambda)\\ \sin(m\lambda)\end{Bmatrix}\sin(\theta)\; d\theta\, d\lambda, \tag{3}$$

we employ the uncertainties of the tidal estimates to derive the Stokes coefficients in a least-squares adjustment via a complete orthogonal decomposition. We do so compelled from the fact that the nodes for which the tidal fit a posteriori unit variance is highest is at least one order of magnitude larger than the minimum a posteriori unit variance over the 2D field. The difference between calculating the Stokes coefficients employing eq. 3 and estimating them in a weighted least-squares adjustment projected on the synthesized fields yields sub-Pa WRMS at expansion degrees pertinent for the reduction of satellite gravimetry observations, that is, 60 or higher. While estimating the Stokes coefficients is computationally more expensive, it offers the opportunity to study the error spectrum as well as the correlations between the harmonic estimates (see Fig. S12). For instance, we note that the estimation uncertainty decreases from zonal to tesseral to sectorial coefficients.

Despite having obtained tidal amplitude estimates on an 0.25° equiangular mesh, there is no need to employ a harmonic expansion to degree 916 (following Barthelmes (2013), it is $\psi_{min} = 4\sin^{-1}\left((1+n_{max})^{-1}\right)$, where n_{max} is the expansion degree and ψ_{min} is the signal half-wavelength). To obtain the necessary expansion degree, we have assessed the WRMS of the post-fit (eq. 2) residuals for each wave. Since surface pressure tides are spatially smoother than ocean bottom pressure tides, they require an expansion to a lower degree. To reach WRMS of 1 Pa the S_1 surface pressure tide needs to be developed to degree 360 as it displays notable correlation with the orography, whereas the S_2 surface pressure tide needs to be developed only to degree 158 to achieve that level of precision. For ocean bottom pressure, the WRMS is still beyond the 1 Pa for expansion degree 180/360 (4.9/2.1 Pa for both S_1 and S_2). However, given the uncertainty of the data based on which the Stokes coefficients were estimated, the spatial correlations thereof, and the fact that harmonic upward continuation greatly diminishes the contribution of high-degree coefficients at low-Earth-orbit satellite altitude, we chose to disseminate all harmonic waves to an expansion degree 360.

Stokes coefficients for atmospheric pressure and ocean bottom pressure tides may be retrieved from Sulzbach et al. (2021).

6. Stokes Coefficients

To assess the total tidal energy per wave nested in the estimated Stokes coefficients ($\overline{C}_{nm}$ and $\overline{S}_{nm}$), we have resorted to absolute spectral methods and especially to the degree variance σ_n^2 as well as the error degree variance $\hat{\sigma}_n^2$ or power spectrum. The fact that the error spectrum of the Stokes coefficients is not isotropic does not allow to express

the total power (see Fig. S12), hence the order and error order variance are studied as well (e.g., Tsoulis & Patlakis, 2013), hereinafter denoted by σ_m^2 and $\hat{\sigma}_m^2$. The $\hat{\sigma}_n^2$ and $\hat{\sigma}_m^2$ are calculated employing the diagonal elements of the Stokes coefficients covariance from a weighted least-squares adjustment. The aforementioned quantities are calculated as follows

$$\begin{aligned} \begin{Bmatrix} \sigma_n^2 \\ \sigma_m^2 \end{Bmatrix} &= \begin{Bmatrix} \sum_{m=0}^{n} \\ \sum_{n=m}^{N} \end{Bmatrix} \left(\overline{C}_{nm}^{2} + \overline{S}_{nm}^{2} \right), \text{and} \\ \begin{Bmatrix} \hat{\sigma}_n^2 \\ \hat{\sigma}_m^2 \end{Bmatrix} &= \begin{Bmatrix} \sum_{m=0}^{n} \\ \sum_{n=m}^{N} \end{Bmatrix} \left(\hat{\sigma}^{2}_{\overline{C}_{nm}} + \hat{\sigma}^{2}_{\overline{S}_{nm}} \right). \end{aligned} \tag{4}$$

6.1. Wind Stress: S_1 & S_2 Amplitudes, Variance Explained by Wave Ensemble, and Degree Variance

References

Barthelmes, F. (2013). Definition of functionals of the geopotential and their calculation from spherical harmonic models. *Scientific Technical Report; 09/02; ISSN 1610-0956*. Retrieved from https://gfzpublic.gfz-potsdam.de/pubman/item/item_104132 doi: 10.2312/GFZ.B103-0902-26

Bierman, G. (2006). *Factorization methods for discrete sequential estimation.* Mineola, N.Y: Dover Publications.

Gelaro, R., McCarty, W., Suárez, M. J., Todling, R., Molod, A., Takacs, L., ... Zhao, B. (2017, July). The modern-era retrospective analysis for research and applications, version 2 (MERRA-2). , *30*(14), 5419–5454. Retrieved from https://doi.org/10.1175/jcli-d-16-0758.1 doi: 10.1175/jcli-d-16-0758.1

Hirvonen, R. A. (1962). *On the statistical analysis of gravity anomalies / by r. a. hirvonen.* Helsinki.

Ray, R. D., & Merrifield, M. A. (2019). The semiannual and 4.4-year modulations of extreme high tides. *Journal of Geophysical Research: Oceans*, *124*(8), 5907-5922. Retrieved from https://agupubs.onlinelibrary.wiley.com/doi/abs/10.1029/2019JC015061 doi: https://doi.org/10.1029/2019JC015061

Ray, R. D., & Poulose, S. (2005). Terdiurnal Surface-Pressure Oscillations over the Continental United States. *Monthly Weather Review*, *133*(9), 2526 - 2534. Retrieved from https://journals.ametsoc.org/view/journals/mwre/133/9/mwr2988.1.xml doi: 10.1175/MWR2988.1

Sneeuw, N. (1994). Global spherical harmonic analysis by least-squares and numerical quadrature methods in historical perspective. *Geophysical Journal International*,

118(3), 707-716. Retrieved from https://onlinelibrary.wiley.com/doi/abs/10.1111/j.1365-246X.1994.tb03995.x doi: https://doi.org/10.1111/j.1365-246X.1994.tb03995.x

Sulzbach, R., Dobslaw, H., & Thomas, M. (2021). *Mass variations induced by ocean tide oscillations (time21).* GFZ Data Services. Retrieved from https://dataservices.gfz-potsdam.de/panmetaworks/showshort.php?id=c90a44a4-ad92-11eb-9603-497c92695674 doi: 10.5880/GFZ.1.3.2021.001

Tsoulis, D., & Patlakis, K. (2013). A spectral assessment review of current satellite-only and combined earth gravity models. *Reviews of Geophysics*, *51*(2), 186-243. Retrieved from https://agupubs.onlinelibrary.wiley.com/doi/abs/10.1002/rog.20012 doi: https://doi.org/10.1002/rog.20012

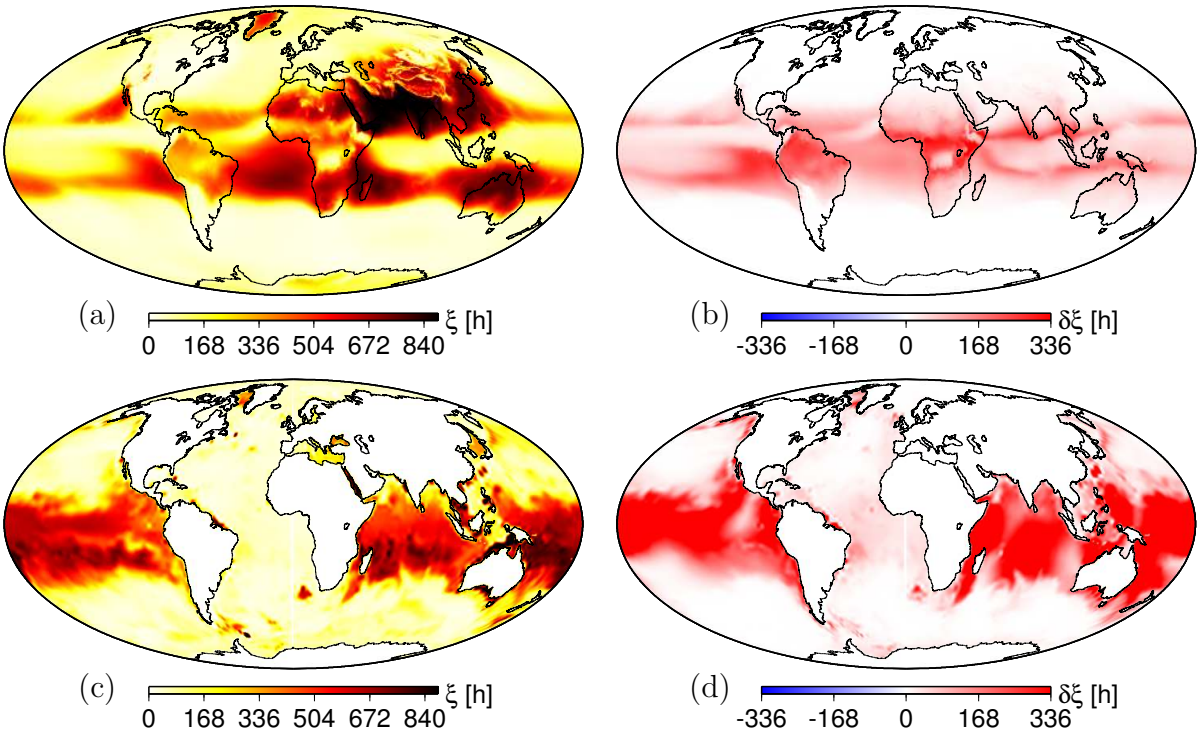

Figure S1: Temporal de-correlation times Surface pressure (upper row) and ocean bottom pressure (lower row) correlation length estimated employing Hirvonen's covariance model (left column). Correlation length difference between the post-tidal-fit pressure residuals raw logs (right column).

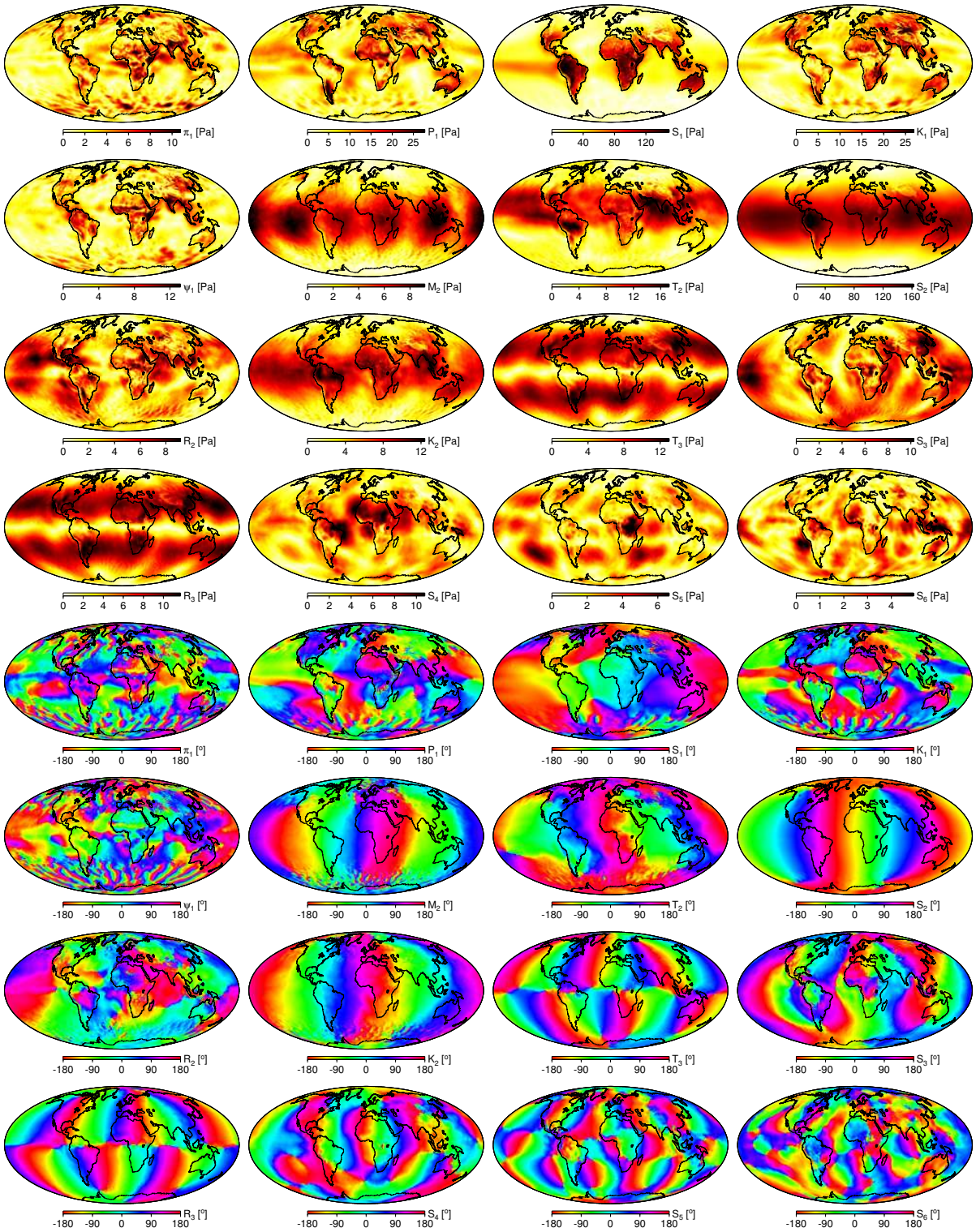

Figure S2: ERA5-derived atmospheric pressure amplitudes and phases.

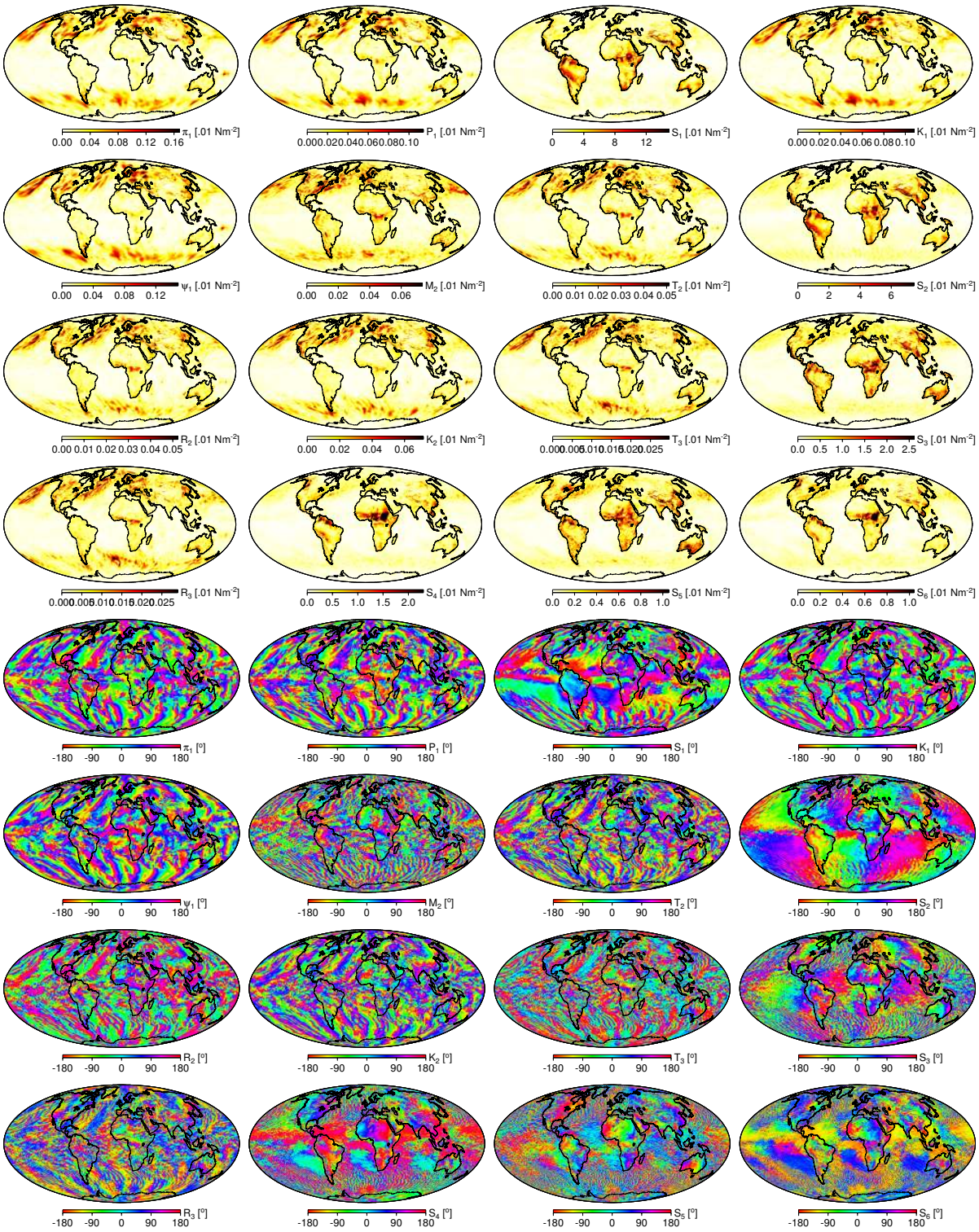

Figure S3: ERA5-derived meridional surface wind stress amplitudes and phases.

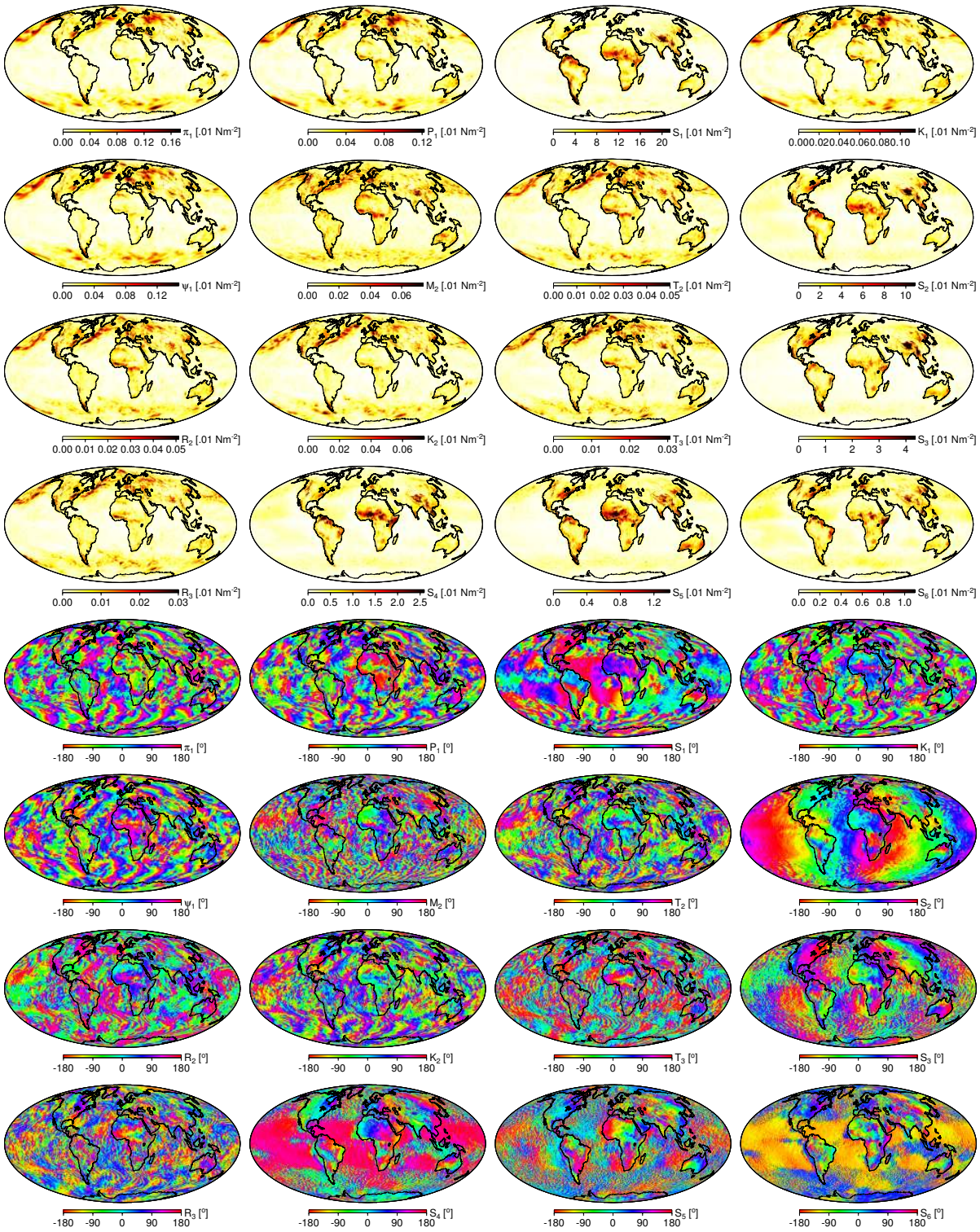

Figure S4: ERA5-derived zonal surface wind stress amplitudes and phases.

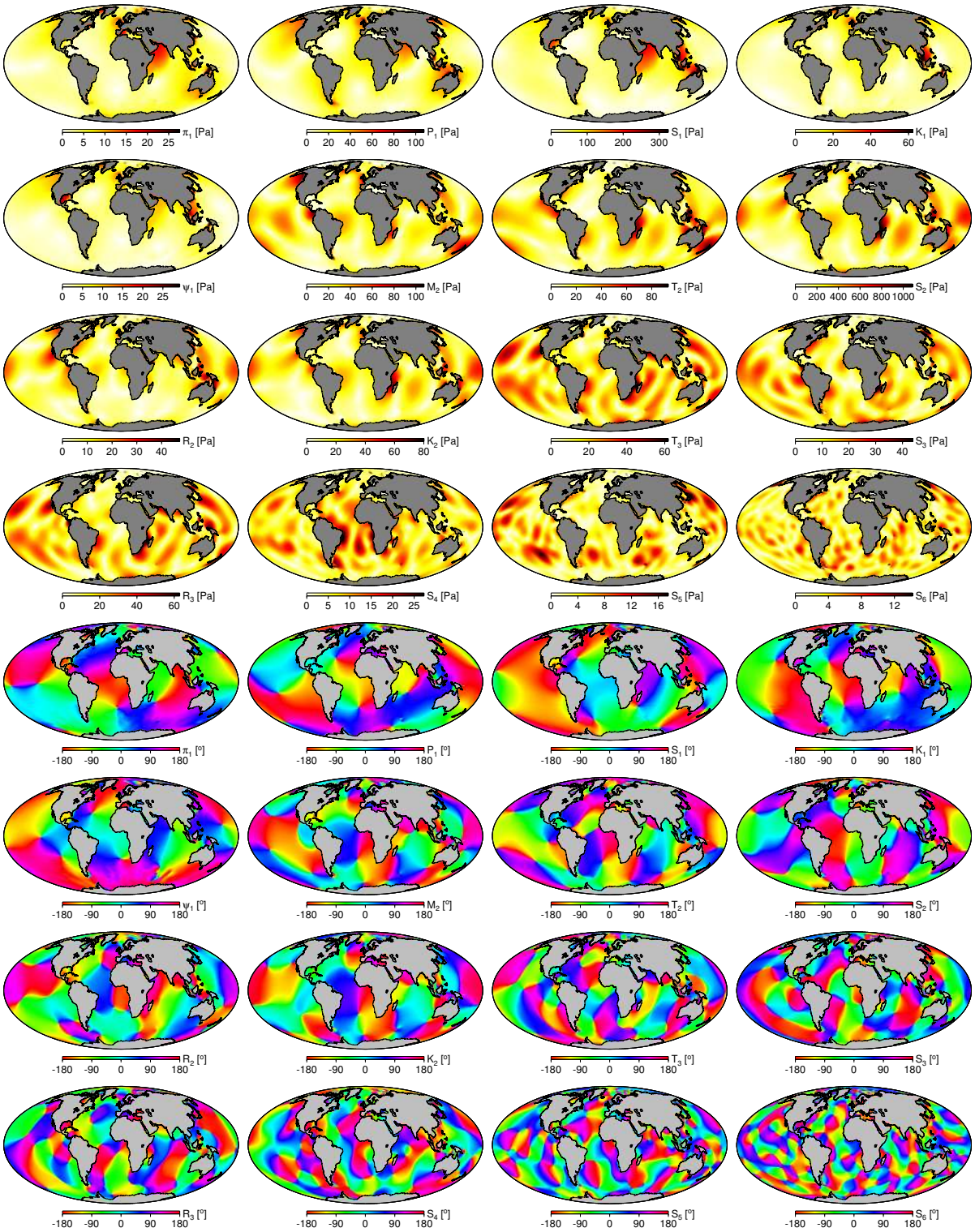

Figure S5: MPIOM-derived ocean bottom pressure amplitudes and phases.

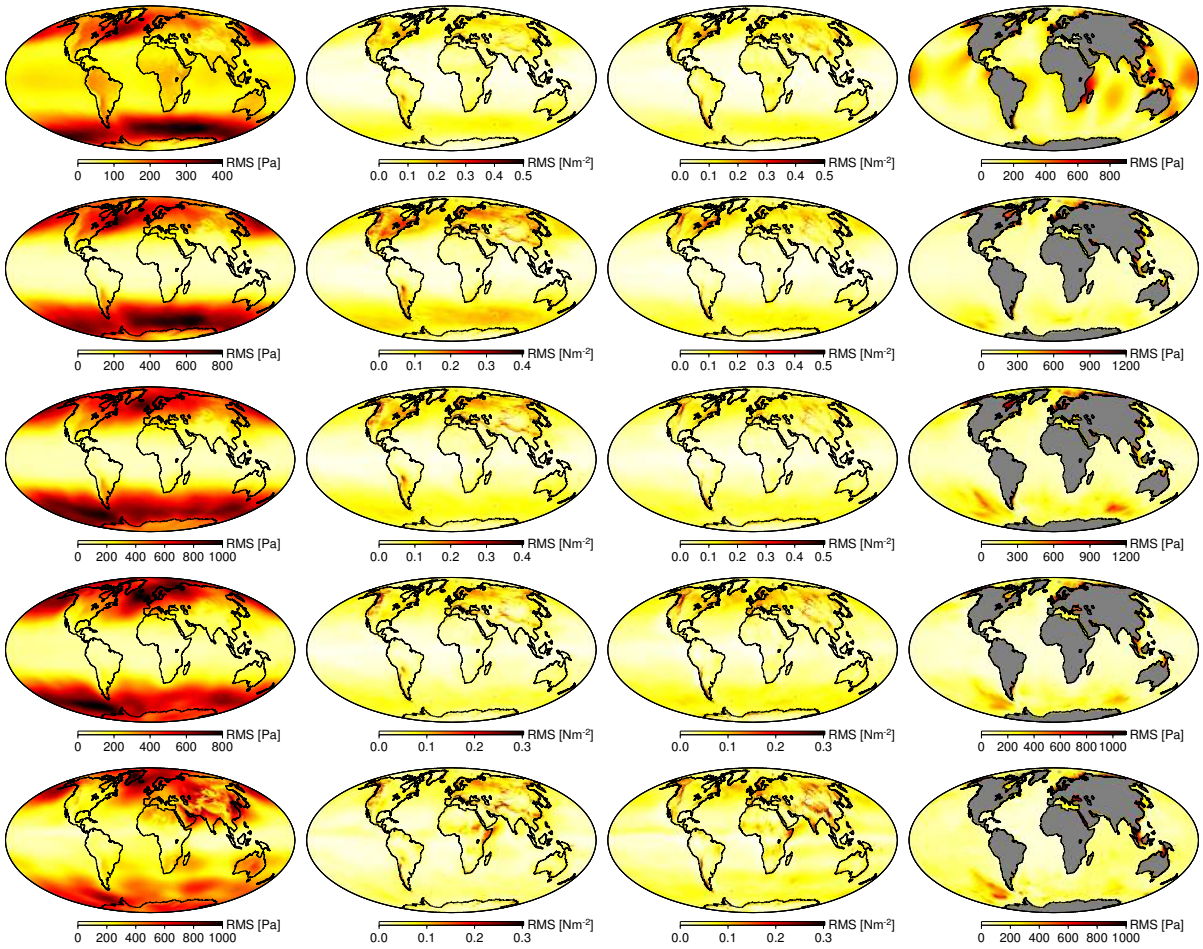

Figure S6: Scatter of band-pass filtered (Butterworth, 6$^{\text{th}}$ order) surface pressure (1$^{\text{st}}$ column), meridional and zonal wind stress (2$^{\text{nd}}$ and 3$^{\text{rd}}$ column, respectively) and ocean bottom pressure series (4$^{\text{th}}$ column). Shown are the RMS of variations in the frequency bands <1 d (1$^{\text{st}}$ row), 1–3 d (2$^{\text{nd}}$ row), 3–10 d (3$^{\text{rd}}$ row), 10–30 d (4$^{\text{th}}$ row), >30 d (5$^{\text{th}}$ row). Note the different colorbar scales.

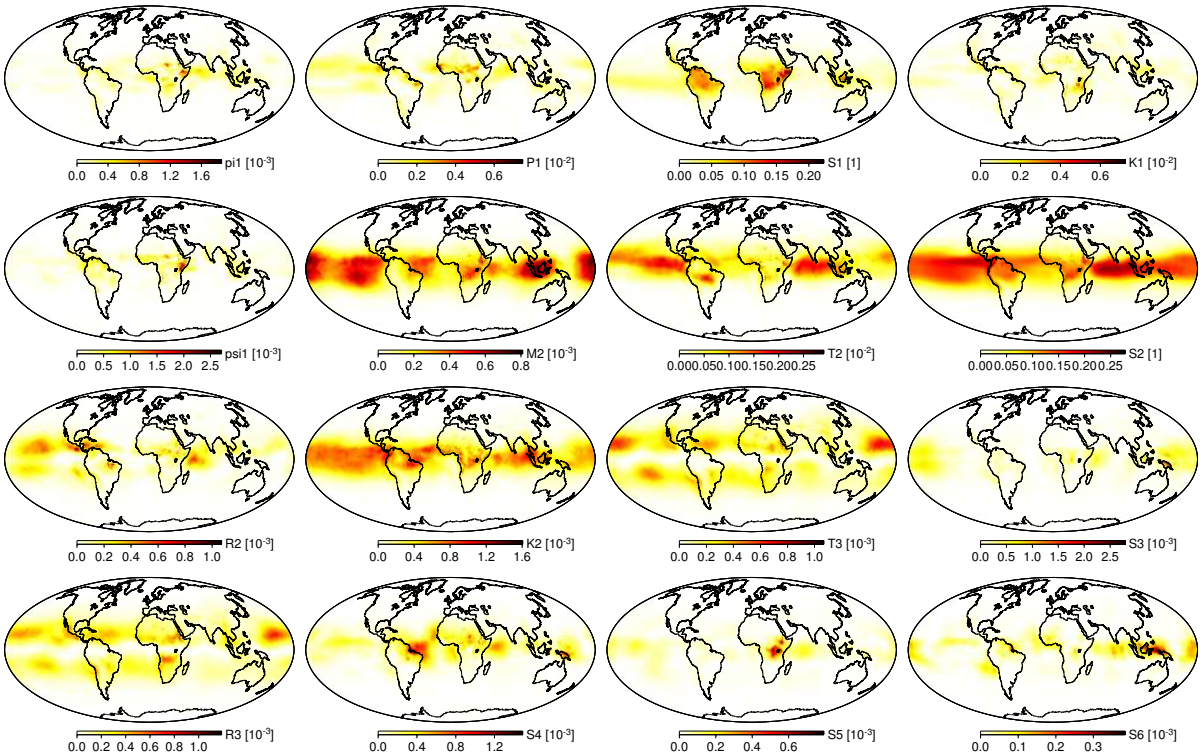

Figure S7: Portion of the atmospheric pressure variance explained by each member of the wave ensemble.

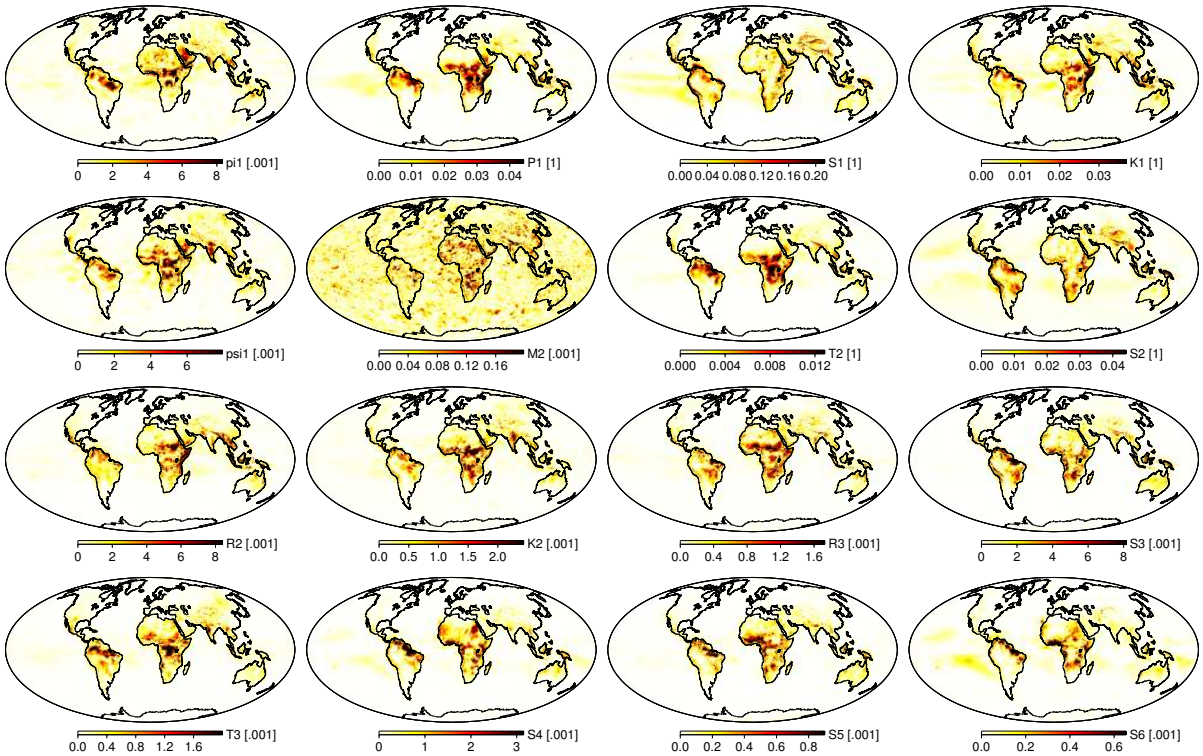

Figure S8: Portion of the meridional wind stress variance explained by each member of the wave ensemble.

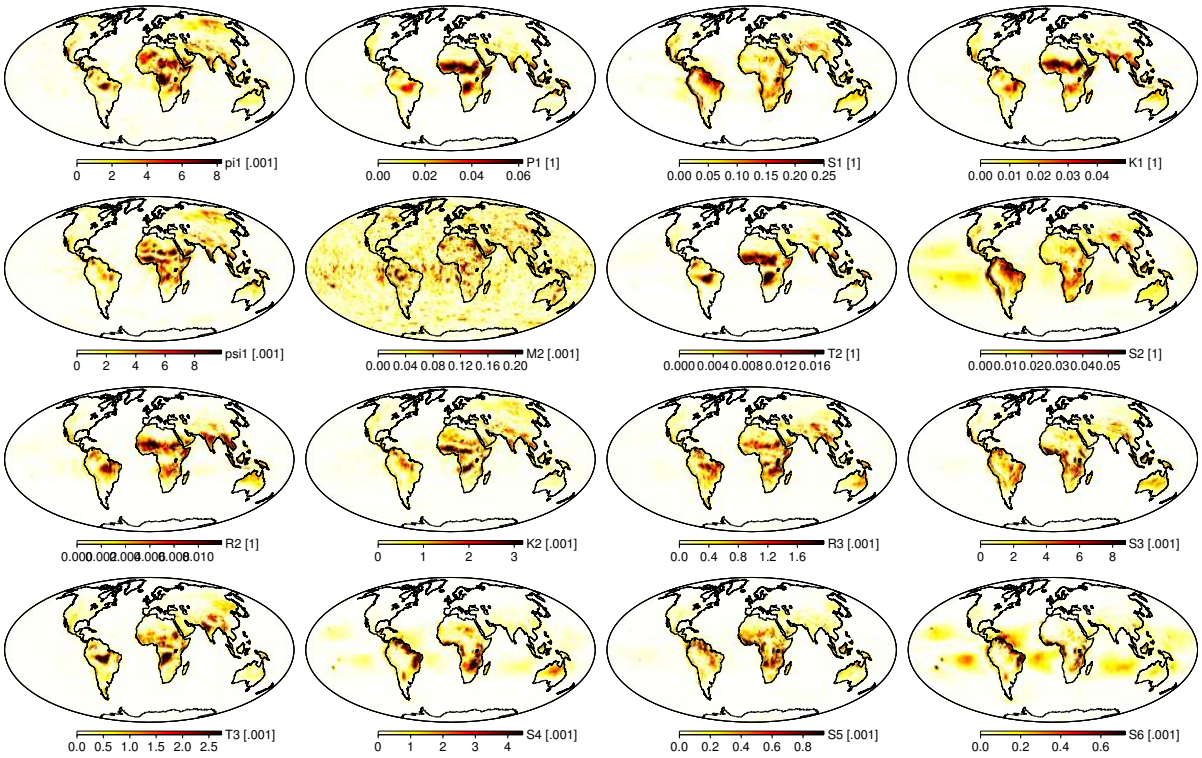

Figure S9: Portion of the zonal wind stress variance explained by each member of the wave ensemble.

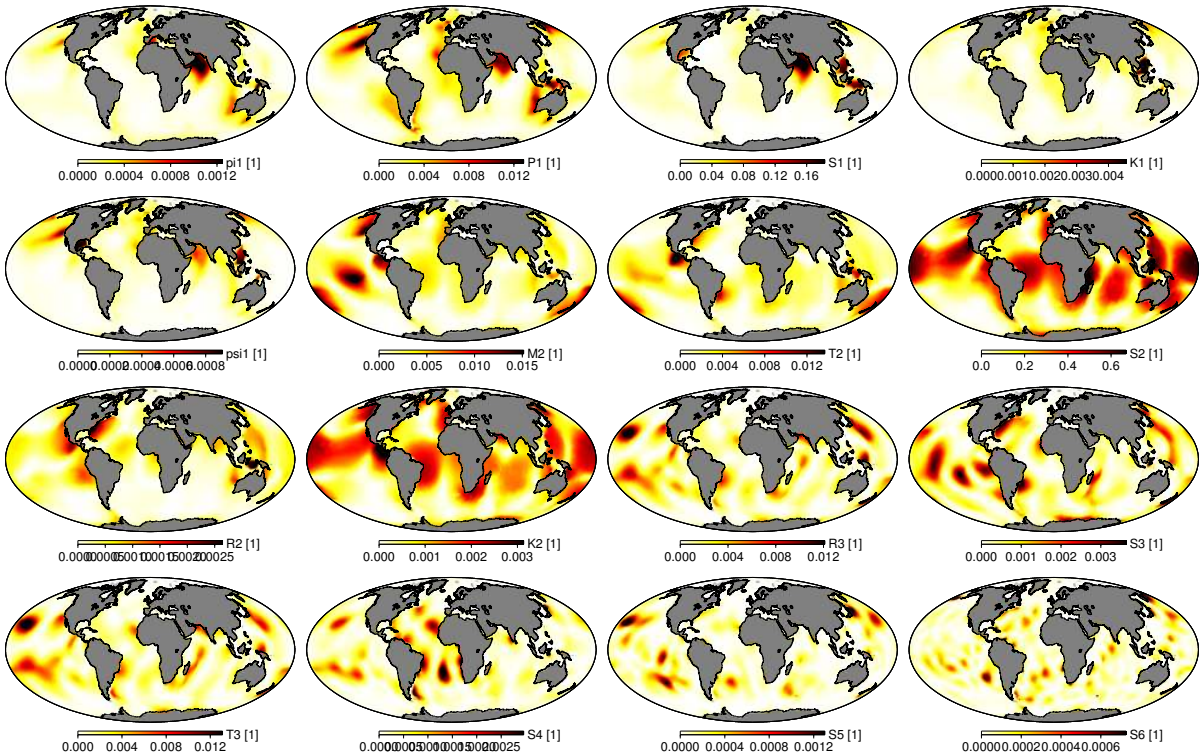

Figure S10: Portion of the ocean bottom pressure variance explained by each member of the wave ensemble.

Figure S11: Signal-to-noise ratio between time-invariant tidal amplitudes and the scatter of time-dependent harmonic coefficients based on ERA5, MERRA2, and ECMWF atmospheric pressure data. To avoid aliasing effects, no harmonics with a frequency higher than 4 cpd were estimated employing 3-hourly ECMWFop series.

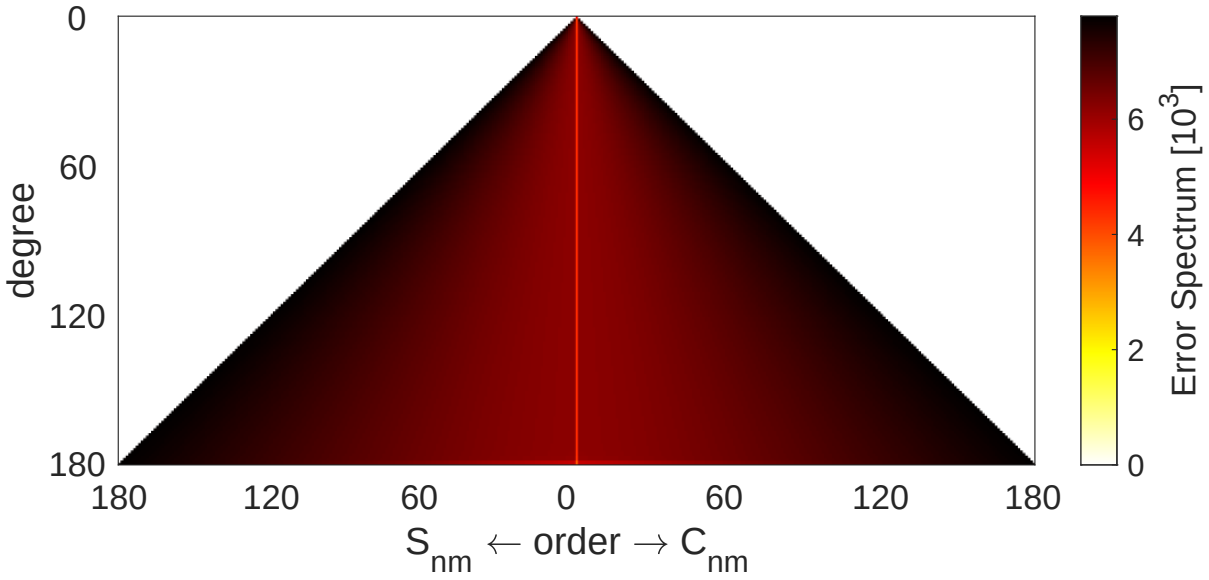

Figure S12: Error spectrum of the Stokes coefficients estimates from the global spherical harmonic analysis of the S_2 atmospheric tide amplitude truncated to degree 180.

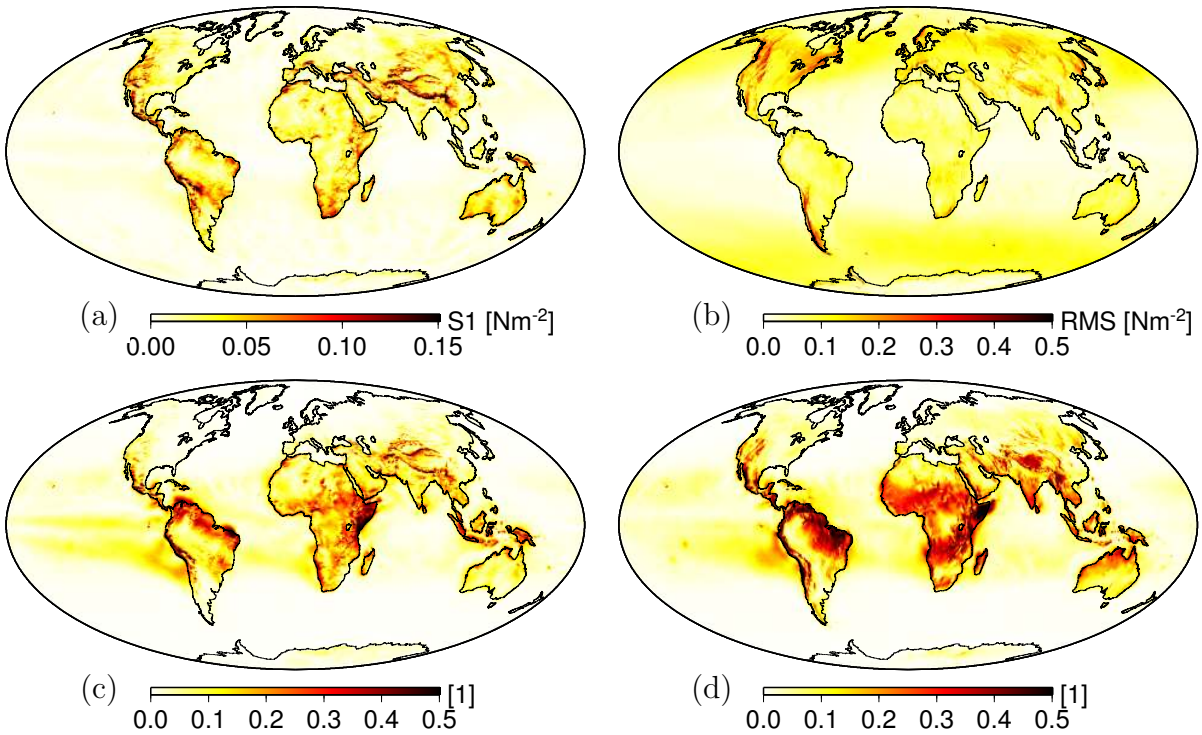

Figure S13: Scatter in the sub-daily frequency band (upper row) and the portion of these variations explained by the waves in Table 1 of the main article (lower row). Depicted are quantities for the meridional wind stress component (left) and the zonal wind stress component (right).

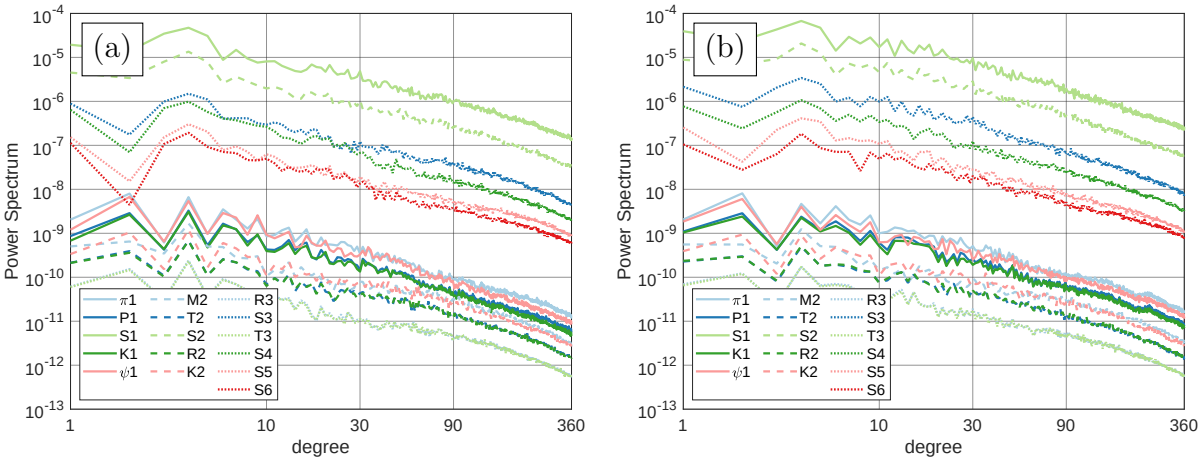

Figure S14: Degree variance of the amplitudes ($A_j = \sqrt{C_j^2 + S_j^2}$) of the most important high-frequency instantaneous meridional (left) and zonal (right) turbulent surface stress tidal waves listed in Table 1 of the main article. Diurnal waves are shown in solid lines, semi-diurnal waves are shown in dashed lines, and waves at the ter-diurnal band or higher are shown in dotted lines.